MODELLISTICA E CALCOLO SCIENTIFICO

M[O]**X**

MODELING AND SCIENTIFIC COMPUTING

Mathematical and numerical modeling of atherosclerotic plaque progression based on fluid-structure interaction

Pozzi, S.; Redaelli, A.; Vergara, C.; Votta, E.; Zunino, P.

Mathematical and numerical modeling of atherosclerotic plaque progression based on fluid-structure interaction

S. Pozzi[1], A. Redaelli[2], C. Vergara[3], E. Votta[2], P. Zunino[1]

September 9, 2020

[1] MOX, Dipartimento di Matematica, Politecnico di Milano
`<silvia.pozzi,paolo.zunino>@polimi.it`
[2] Dipartimento di Elettronica, Informazione e Bioingegneria, Politecnico di Milano
`<alberto.redaelli,emiliano.votta>@polimi.it`
[3] LaBS, Dipartimento di Chimica, Materiali e Ingegneria Chimica "Giulio Natta,
Politecnico di Milano
`christian.vergara@polimi.it`

Abstract

In this work we propose a mathematical and numerical model to describe the early stages of atherosclerotic plaque formation, which is based on the interaction of processes with different spatial and temporal scales. A fluid-structure interaction problem, used to describe the cardiovascular mechanics arising between blood and the artery wall, is coupled to a set of differential problems describing the evolution of solute concentrations. In order to manage the *multiscale-in-space* nature of the involved processes, we propose a suitable numerical strategy based on the splitting and sequential solution of the coupled problem. We present some preliminary numerical results and investigate the effects of geometry, model parameters and coupling strategy on plaque growth.

1 Introduction

Atherosclerosis is a vascular disease affecting the artery wall, leading to the chronic inflammation of its inner layers and to the development of an atherosclerotic plaque or atheroma [39, 18, 30]. The growth of plaque induces a narrowing

1

of the arterial lumen, causing its partial or total occlusion. Possible consequences include the blockage of distal vessels caused by fragments generated by plaque rupture or the formation and detachment of a thrombus. Both phenomena can lead to a lack of blood flow to the distal tissues, and thus to severe cardiovascular events such as myocardial or cerebral ischemia and stroke.

The mechanisms leading to plaque development and growth are not yet fully understood and are still an active area of research. It is however well-accepted that the role of the endothelium, the single layer of cells constituting the interface between the lumen and the artery wall, is crucial to the onset of plaque. Indeed, it acts as a transport barrier controlling the flow of molecular and cellular species, whose permeability depends on hemodynamic factors [46, 28, 33, 3]. In the case of atherosclerosis, a dysfunction of the endothelium caused by a disturbed flow characterized by a low and oscillating *wall shear stress* (WSS), increases the infiltration of species into the artery wall. For this reason, plaques typically occur at curved or bifurcating segments, where WSS is low and oscillating. Predominant sites for plaque formation in humans include coronary arteries and carotids.

The events that lead to early atherosclerotic plaque formation can be summarized as follows [18]:

1. In regions of perturbed, recirculating flow and correspondingly low and oscillating WSS, *low-density lipoprotein* (LDL) present in the bloodstream crosses the endothelium and penetrates into the artery wall;

2. LDL, once in the artery wall, undergoes oxidative modification by endothelial cells, macrophages and smooth muscle cells;

3. Modified LDL causes the onset of an inflammatory process, releasing monocyte attracting factors;

4. Monocytes migrate from the bloodstream into the artery wall, where they differentiate into macrophages;

5. Due to the ingestion of oxidized LDL, macrophages differentiate into foam cells;

6. Accumulation of foam cells further stimulates the inflammation, and leads to the growth of a subendothelial plaque.

A schematic representation of these processes is reported in Figure 1.

Given the severe cardiovascular consequences caused by atherosclerosis, the study of the formation and evolution of plaques is of utmost importance. In this framework, the use of computational modeling focusing on the mathematical and numerical description of plaque progression is gaining relevance as a tool to study its mechanobiological processes and identify possible prevention and treatment strategies. Comprehensive overviews of existing models can be found in [37, 2].
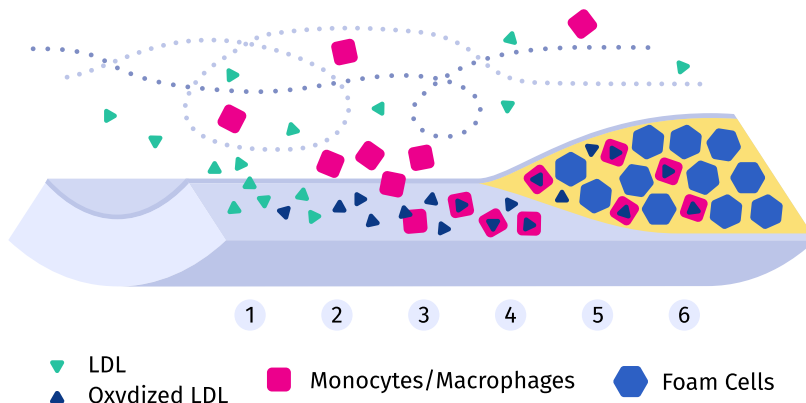
Figure 1: Schematic view of plaque formation and progression. LDL penetrates into the artery wall (1), where it oxydizes (2); Monocytes migrate from the bloodstream (3) and ingest oxydized LDL (4); Macrophages differentiate into foam cells (5) and accumulate 6) .

A mathematical model of plaque growth should account for both the *multiscale-in-space* and *in-time* nature of the problem. Indeed, it involves both macroscopic cardiovascular processes, such as blood dynamics at the bifurcation, with a characteristic time of 1 second (the mean duration of the cardiac cycle), as well as molecular and cellular events, which lead to plaque growth in a time horizon of months to years.

In order to model molecular and cellular phenomena, a large number of studies considers a macroscopic description by means of suitable partial differential equations (PDEs) [4, 16, 11, 23, 45, 6, 43, 40], whereas other works consider different approaches, such as agent-based modeling [12] or fluid-solid-growth modeling [20]. As for macroscopic events, among the existing models many consider blood dynamics in rigid walls [4, 31, 16, 11, 12, 40], whereas others consider compliant vessels in the framework of fluid-structure interaction (FSI) [45, 43].

Regarding the interaction of the different spatial scales, most studies introduce a *macro-to-micro* scales feedback by adopting a relationship linking WSS and the permeability of the endothelium [4, 16, 43, 12, 40] or linking WSS and growth itself [31, 1]. On the other hand, the *micro-to-macro* scales feedback can be expressed in terms of phenomenological growth laws [47, 4, 16, 11], relating species concentrations to plaque thickening, or by including a growth tensor in the vessel wall dynamics to account for the plaque development [45, 43].

We point out that, concerning the interaction of different time scales, no specific techniques related to modeling atherosclerosis development has been considered so far. An approach has been to artificially increase model parameters in order to accelerate plaque growth [43, 12]. A different method has been proposed in [31, 1], in which several growth stages are simulated sequentially in order to describe a longer time horizon. Here, we follow the strategy proposed

in [38] that splits the long and short time scales problems at the numerical level.

Starting from the studies cited above, in this work we propose a mathematical model for plaque initiation and progression in which we aim at providing:

i. A detailed description of hemodynamics, which plays a crucial role in plaque onset and growth;

ii. A two-way coupling between *micro* and *macro* spatial scales;

iii. A coupling between different characteristic times (seconds for hemodynamics, years for plaque progression).

Our mathematical model is based on the interaction between an FSI problem, elliptic PDEs for the evolution of LDL and macrophages, and an ODE for foam cells. We adopt a two-way feedback between *micro* and *macro* scales based on WSS and a growth law. At the numerical level, we propose a strategy similar to [31] to deal with the *multiscale-in-time* nature of the problem.

The structure of the work is as follows. In Sect. 2 we detail the mathematical model for plaque development, whereas in Sect. 3 we discuss the numerical strategy introduced for the approximation. Finally, in Sect. 4 we present several numerical results.

2 Mathematical models

2.1 Overview of the method

The mathematical model we present here is built upon the coupling of two sets of differential problems, modeling processes characterized by different time scales. The *short time scales* model describing blood dynamics and its interaction with the vessel wall is represented by the FSI problem, with ($\boldsymbol{u}$, p, $\boldsymbol{d}$) the unknown fluid velocity, fluid pressure and vessel wall displacement. Instead, the *long time scales* model describing the accumulation of species, inflammation, and plaque growth is composed by 3 problems interacting with one another. In particular, we consider two time dependent diffusion-reaction (DR) problems for the concentrations c_{LDL} and c_M of LDL and macrophages, respectively [4, 43], and one ordinary differential equation (ODE) for the concentration of foam cells c_{FC} [16].

The interaction between these two sets of problems determines the unknown plaque growth function $\boldsymbol{d}_G$. In particular, the effect of short time scales on the long ones is provided by function $g_1(\boldsymbol{u})$ defined as the time-averaged *WSS* (*TAWSS*), which influences the permeabilities to LDL and macrophages [4, 43] (*macro-to-micro* feedback). On the other side, the effect of long time scales on the short ones is provided by the growth function $\boldsymbol{d}_G$ through a suitable function of the foam cells concentrations $g_2 = g_2(c_{FC})$ (*micro-to-macro* feedback). In Figure 2 we report a schematic representation of the mathematical model. We

4

highlight the dependency of the fluid and structure domains Ω_f and Ω_s on the plaque growth $\boldsymbol{d}_G$.

Short time scale model

$$(\boldsymbol{u}, p, \boldsymbol{d}) = \mathcal{FS}\left(\Omega_f\left(\boldsymbol{d}_G\right), \Omega_s\left(\boldsymbol{d}_G\right)\right)$$

$g_2(c_{FC}) = \boldsymbol{d}_G$

$g_1(\boldsymbol{u}) = TAWSS$

Long time scale model

$$c_{LDL} = \mathcal{DR}\left(TAWSS; \Omega_s\left(\boldsymbol{d}_G\right)\right)$$
$$c_M = \mathcal{DR}\left(TAWSS, c_{LDL}, c_{FC}; \Omega_s\left(\boldsymbol{d}_G\right)\right)$$
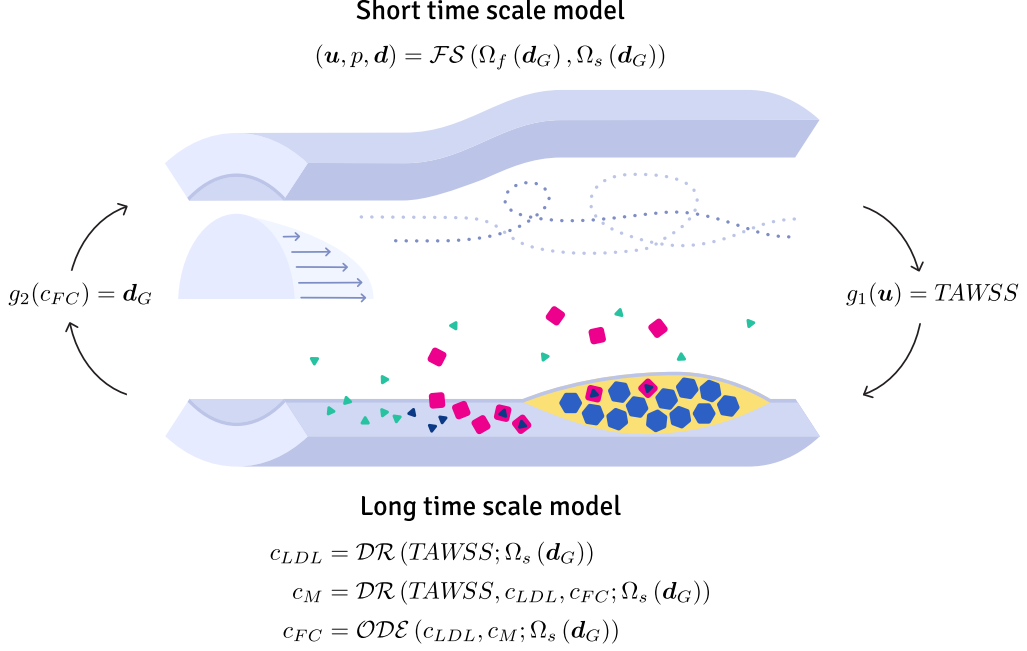$$c_{FC} = \mathcal{ODE}\left(c_{LDL}, c_M; \Omega_s\left(\boldsymbol{d}_G\right)\right)$$

Figure 2: Schematic representation of the mathematical model of plaque progression.
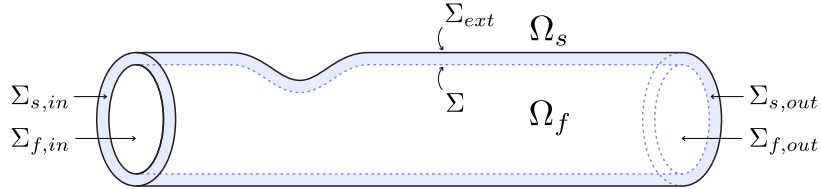

Figure 3: Fluid and structure computational domains.

2.2 FSI problem

Referring to Figure 3, we consider the time-varying domains $\Omega_f^t \subset \mathbb{R}^3$ and $\Omega_s^t \subset \mathbb{R}^3$, representing the lumen of the artery and its wall, respectively. We neglect the heterogeneous and multi-layered nature of the artery wall and describe it as a single layer structure. Let Σ^t be the endothelium, that is the interface between the fluid and structure domains, and Σ_{ext}^t be the outer surface of the artery wall.

The fluid problem is stated in an *Arbitrary Lagrangian-Eulerian* (ALE) framework [25, 17]. The ALE map is defined by an appropriate lifting of the

structure displacement $\boldsymbol{d}$ at the interface Σ^t, and defines the fluid domain displacement $\boldsymbol{d}_f$ and velocity $\boldsymbol{u}_f = \dot{\boldsymbol{d}}_f$. In this work we have chosen the standard harmonic extension lifting. A Lagrangian approach is adopted for the structure problem, whose quantities are denoted by $\widehat{}$.

Accordingly, the coupled problem at each time $t > 0$ reads: find fluid velocity $\boldsymbol{u} = \boldsymbol{u}(t, \boldsymbol{x})$, fluid pressure $p = p(t, \boldsymbol{x})$, structure displacement $\boldsymbol{d} = \boldsymbol{d}(t, \boldsymbol{x})$ and fluid domain displacement $\boldsymbol{d}_f = \boldsymbol{d}_f(t, \boldsymbol{x})$ such that:

$$\rho_f \left(\delta_t \boldsymbol{u} + (\boldsymbol{u} - \boldsymbol{u}_f) \cdot \nabla \boldsymbol{u} \right) - \nabla \cdot \boldsymbol{T_f}(\boldsymbol{u}, p) = \boldsymbol{0} \quad \text{in } \Omega_f^t(\boldsymbol{d}, \boldsymbol{d}_G), \tag{1a}$$

$$\nabla \cdot \boldsymbol{u} = 0 \quad \text{in } \Omega_f^t(\boldsymbol{d}, \boldsymbol{d}_G), \tag{1b}$$

$$\boldsymbol{u} = \partial_t \boldsymbol{d} \quad \text{on } \Sigma^t(\boldsymbol{d}, \boldsymbol{d}_G), \tag{1c}$$

$$\boldsymbol{T_f}(\boldsymbol{u}, p)\boldsymbol{n} = \boldsymbol{T_s}(\boldsymbol{d})\boldsymbol{n} \quad \text{on } \Sigma^t(\boldsymbol{d}, \boldsymbol{d}_G), \tag{1d}$$

$$\rho_s \partial_{tt} \widehat{\boldsymbol{d}} - \nabla \cdot \widehat{\boldsymbol{T}}_s(\widehat{\boldsymbol{d}}) = \boldsymbol{0} \quad \text{in } \widehat{\Omega}_s(\boldsymbol{d}_G), \tag{1e}$$

$$\widehat{\boldsymbol{d}}_f = \widehat{\boldsymbol{d}} \quad \text{on } \widehat{\Sigma}, \tag{1f}$$

$$-\Delta \widehat{\boldsymbol{d}}_f = \boldsymbol{0} \quad \text{in } \Omega_f^t(\boldsymbol{d}, \boldsymbol{d}_G), \tag{1g}$$

together with suitable initial and boundary conditions, and where ρ_f and ρ_s are the fluid and structure densities, $\boldsymbol{n}$ is the outward unit normal vector, and δ_t represent the ALE time derivative. The dependency of the domains on the growth function $\boldsymbol{d}_G$ will be specified below.

The ALE map introduces the geometric coupling condition (1f), while (1b) - (1c) represent the kinematic and dynamic fluid-structure interface conditions, respectively.

In Equation (1a), $\boldsymbol{T}_f = \mu_f(\nabla \boldsymbol{u} + (\nabla \boldsymbol{u})^T)\boldsymbol{n} - p\boldsymbol{I}$ is the fluid Cauchy stress tensor, where μ_f is the fluid viscosity. In Equation (1e), $\widehat{\boldsymbol{T}}_s$ is the solid first Piola-Kirkhhoff stress tensor. In this work, for the sake of simplicity in order to focus on the coupling with the *long time scales* model, we consider a linear elastic material:

$$\boldsymbol{T}_s(\boldsymbol{d}) = \lambda tr(\boldsymbol{\varepsilon})\boldsymbol{I} + 2\mu_s \boldsymbol{\varepsilon},$$

where λ and μ_s are Lamé's parameters and $\boldsymbol{\varepsilon}(\boldsymbol{d}) = \frac{1}{2}(\nabla \boldsymbol{d} + (\nabla \boldsymbol{d})^T)$ is the strain tensor.

Boundary conditions We prescribe for the structure domain problem on the inlet and outlet rings $\widehat{\Sigma}_{s,in}$ and $\widehat{\Sigma}_{s,out}$ a tangential homogeneous Neumann boundary condition to allow movement of the inlet and outlet in the tangential directions $\boldsymbol{\tau}_j$, $j = 1, 2$, and a homogeneous Dirichlet boundary condition in the normal direction:

$$(\widehat{\boldsymbol{T}}_s \widehat{\boldsymbol{n}}) \cdot \widehat{\boldsymbol{\tau}}_j = \boldsymbol{0}, \quad j = 1, 2 \qquad \text{on } \widehat{\Sigma}_{s,in} \cup \widehat{\Sigma}_{s,out}, \tag{2a}$$

$$\widehat{\boldsymbol{d}} \cdot \widehat{\boldsymbol{n}} = \boldsymbol{0} \qquad \text{on } \widehat{\Sigma}_{s,in} \cup \widehat{\Sigma}_{s,out}. \tag{2b}$$

Accordingly, for the fluid domain problem we prescribe on the inlet and outlet artificial sections $\widehat{\Sigma}_{f,in}$ and $\widehat{\Sigma}_{f,out}$ a tangential homogeneous Neumann condition and a normal homogeneous Dirichlet condition:

$$\nabla \widehat{\boldsymbol{d}}_f \widehat{\boldsymbol{n}} \cdot \widehat{\boldsymbol{\tau}}_j = \boldsymbol{0}, \quad j = 1, 2 \qquad \text{on } \widehat{\Sigma}_{f,in} \cup \widehat{\Sigma}_{f,out}, \qquad (3a)$$

$$\widehat{\boldsymbol{d}}_f \cdot \widehat{\boldsymbol{n}} = \boldsymbol{0} \qquad \text{on } \widehat{\Sigma}_{f,in} \cup \widehat{\Sigma}_{f,out}. \qquad (3b)$$

On the fluid inlet surface $\Sigma_{f,in}^t$ we consider a flow rate condition:

$$\int_{\Sigma_{f,in}^t} \boldsymbol{u} \cdot \boldsymbol{n} \, d\sigma = Q_{in}(t).$$

To prescribe the previous condition, a parabolic velocity profile defined in the largest circle immersed in $\Sigma_{f,in}^t$ has been selected in order to deal with a Dirichlet boundary condition:

$$\boldsymbol{u} = \boldsymbol{g}_{in} \qquad \text{on } \Sigma_{f,in}^t, \qquad (4)$$

with $\int_{\Sigma_{f,in}^t} \boldsymbol{g}_{in} \cdot \boldsymbol{n} \, d\sigma = Q_{in}$.

To avoid numerical reflections given by the truncation of the computational domain, we prescribe on the fluid outlet $\Sigma_{f,out}^t$ a resistance absorbing boundary condition [36]

$$R \int_{\Sigma_{f,out}^t} \boldsymbol{u} \cdot \boldsymbol{n} \, d\sigma + \frac{1}{A} \int_{\Sigma_{f,out}^t} \boldsymbol{T}_f \boldsymbol{n} \cdot \boldsymbol{n} \, d\sigma = P_{ext},$$

with $A = |\Sigma_{f,out}^t|$ the lumen outlet area and P_{ext} the external pressure, together with homogeneous Neumann conditions for the tangential directions. The value of resistance R is computed as [34]

$$R = \sqrt{\frac{\rho_f \beta}{2} \frac{1}{A^{3/4}}},$$

where $\beta = \frac{h_s E}{(1 - \nu^2)} \frac{\pi}{A}$, h_s is a characteristic value for the structure thickness, and E and ν are the Young modulus and the Poisson ratio of the vessel wall.

On the external surface $\widehat{\Sigma}_{ext}$ we prescribe a Robin boundary condition to model the elastic support of the surrounding tissues:

$$\alpha \widehat{\boldsymbol{d}} + \widehat{\boldsymbol{T}}_s(\widehat{\boldsymbol{d}}) \widehat{\boldsymbol{n}} = P_{ext} \widehat{\boldsymbol{n}} \qquad \text{on } \widehat{\Sigma}_{ext}.$$

2.3 Solute differential problems

The differential problems accounting for the interaction of molecules and cellular species leading to the growth of plaque in the artery wall are solved in the structure domain Ω_s^t. As in the case of the FSI problem, the artery wall is

described as a single layer structure. The endothelium Σ^t is treated as a semi-permeable membrane, which allows the infiltration of solutes from blood into the artery wall. All other surfaces are considered impermeable, thus inhibiting the influx or efflux of solutes.

We consider three differential problems to compute the concentrations of LDL, macrophages and foam cells, respectively. The subscript $_M$ refers to both monocytes and macrophages, as in this model we assume that monocytes that enter the artery wall from blood differentiate instantly into macrophages. We highlight the dependency of some parameters on other unknowns. The precise definitions of such dependencies will be detailed in the next subsection.

The evolution of LDL and macrophages in the artery wall is modeled as a diffusion-reaction problem.

$$\partial_t c_{LDL} - \nabla \cdot (D_{LDL} \nabla c_{LDL}) + r_{ox} c_{LDL} = 0 \qquad \text{in } \Omega_s^t(\boldsymbol{d}_G), \qquad (5a)$$

$$\partial_t c_M - \nabla \cdot (D_M(c_{FC}) \nabla c_M) + (r_{ox} c_{LDL}) c_M = 0 \qquad \text{in } \Omega_s^t(\boldsymbol{d}_G), \qquad (5b)$$

where D_{LDL} and D_M are the diffusion coefficients of LDL and macrophages, respectively, and r_{ox} is the rate of oxidation of LDL. Both diffusion-reaction problems are equipped with a Robin condition at the interface Σ

$$\zeta_{LDL}(\boldsymbol{u}) c_{LDL} - D_{LDL} \nabla c_{LDL} \cdot \boldsymbol{n} = -\zeta_{LDL}(\boldsymbol{u}) c_{LDL,f} \qquad \text{on } \Sigma^t(\boldsymbol{d}, \boldsymbol{d}_G), \qquad (6a)$$

$$\zeta_M(\boldsymbol{u}) c_M - D_M \nabla c_M \cdot \boldsymbol{n} = -\zeta_M(\boldsymbol{u}) c_{M,f} \qquad \text{on } \Sigma^t(\boldsymbol{d}, \boldsymbol{d}_G), \qquad (6b)$$

where ζ_{LDL} and ζ_M are the local permeabilities to LDL and monocytes, respectively, through the endothelium. These conditions account for the equilibrium with the fluid concentrations, which are here supposed to be known constants ($c_{LDL,f}$, $c_{M,f}$), and control the influx of LDL and monocytes from the blood to the artery wall through the endothelium Σ.

Finally, the evolution of foam cells is modeled as an ordinary differential equation:

$$\partial_t c_{FC} = r_{ox} c_{LDL} c_M \qquad \text{in } \Omega_s^t(\boldsymbol{d}_G). \qquad (7)$$

The source term in (7) corresponds to the reaction term in (5b), and describes the differentiation of macrophages into foam cells as they absorb oxidized LDL [11]. Foam cells do not migrate into the artery wall from blood, as they are created in the artery wall, so a no-flux condition is imposed on Σ.

$$\nabla c_{FC} \cdot \boldsymbol{n} = \boldsymbol{0} \qquad \text{on } \Sigma^t(\boldsymbol{d}, \boldsymbol{d}_G).$$

Regarding the remaining boundaries, it is assumed that the external boundary Σ_{ext}^t of the artery wall is impermeable, so a homogeneous Neumann condition is prescribed for all species. The same condition is imposed on the inlet and outlet surfaces $\Sigma_{s,in}^t$ and $\Sigma_{s,out}^t$.

2.4 Model parameters

Diffusivity We consider a constant diffusion coefficient D_{LDL} for LDL, while that for monocytes/macrophages D_M is computed as a function of the concentration of foam cells c_{FC} [45]

$$D_M = D_{M,h} + (D_{M,d} - D_{M,h}) \, e^{-a_1 c_{FC}}, \tag{9}$$

where $D_{M,h}$ is the diffusion coefficient in the healthy wall, with no foam cells present, and $D_{M,d}$ in the diseased artery wall, occupied fully by plaque. Being $D_{M,d} > D_{M,h}$ we assume that the diffusivity of macrophages is increased as plaque grows. a_1 is a constant coefficient used to modulate the intensity of the change of diffusivity.

Endothelial permeability Medical evidence shows that regions subject to low and oscillating *WSS* are more likely to develop atheromatous plaques [42, 8, 29, 3]. On the contrary, high *WSS* regions appear to be protected from atherosclerosis [5, 44, 29]. Accordingly, the endothelium has been shown to behave differently in response to altered flow patterns, by changing its permeability to blood solutes. We incorporate this phenomenon in the model by considering values of permeability that are *WSS*-dependent.

In previous works [4, 43], a *WSS*-permeability relationship was considered for LDL. In addition to this choice, we consider a similar *WSS*-permeability relationship to describe also the influx of monocytes. This choice is justified by several *in-vitro* and *in-vivo* works showing an increased adhesion and infiltration of monocytes in low and oscillating *WSS* regions [7, 26, 14, 10, 9].

We employ the same relationship proposed in [43] for the permeabilities to LDL and monocytes. Introducing the time-averaged *WSS* (*TAWSS*) acting on the endothelium Σ

$$TAWSS = \frac{1}{T} \int_0^T \mu_f \sum_{j=1}^2 \sqrt{\left(\left(\nabla \boldsymbol{u} + (\nabla \boldsymbol{u})^T \right) \boldsymbol{n} \cdot \boldsymbol{\tau}_j \right)^2} \, dt, \tag{10}$$

where T is the cardiac cycle length and $\boldsymbol{\tau}_j$ are the tangential unit vectors, the values of $\zeta_{LDL} = \zeta_{LDL}(t, \boldsymbol{x})$ and $\zeta_M = \zeta_M(t, \boldsymbol{x})$ in (6) are computed as functions of *TAWSS* as follows:

$$\zeta_* = \frac{1}{ln(2)} \, ln \left(1 + \frac{a_{*,1}}{TAWSS + a_{*,2}} \right) \zeta_*^{ref} = \frac{1}{ln(2)} \, ln \left(1 + \frac{a_{*,1}}{g_1(\boldsymbol{u}) + a_{*,2}} \right) \zeta_*^{ref}, \tag{11}$$

where $* = LDL, M$. ζ_{LDL}^{ref} and ζ_M^{ref} are reference values of permeability to LDL and monocytes, respectively. To highlight the dependency on the fluid velocity $\boldsymbol{u}$, we have set

$$g_1(\boldsymbol{u}) = TAWSS. \tag{12}$$

The calibration of parameters $a_{LDL,1}$, $a_{LDL,2}$, $a_{M,1}$ and $a_{M,2}$ will be addressed in Section 4. Relationship (11) is a monotonically decreasing function of *TAWSS*,

so that a higher permeability is assigned to regions of the endothelium subject to low *TAWSS*. Relationships accounting also for the oscillatory nature of *WSS* are currently under study.

2.5 Growth function

We assume that the growth of plaque is due to the accumulation of foam cells in the artery wall. The displacement of the interface Σ^t due to growth function $\boldsymbol{d}_G$ is computed with respect to the reference initial configuration $\widehat{\Sigma}$. In particular, we propose the following incremental growth law

$$\boldsymbol{d}_G = g_2(c_{FC}) = \int_0^t \frac{1}{|\Gamma(t, \boldsymbol{x})|} \left(\int_{\Gamma(t, \boldsymbol{x})} \kappa \dot{c}_{FC}(\tau, \boldsymbol{x})\, d\gamma \right) \boldsymbol{n}(\tau, \boldsymbol{x}) d\tau, \quad (13)$$

where $\boldsymbol{n}$ is the normal direction to the interface Σ and κ is a parameter regulating the growth rate [47]. The previous relationship computes the mean line integral of the time variation of the foam cells concentration $\dot{c}_{FC}$ across the vessel wall thickness Γ^t (see Figure 4) and assumes that this produces an internal growth towards the vessel lumen. This is a reasonable assumption for the first stages of plaque formation. Since growth function $g_2(c_{FC})$ represents an accumulation, the integral over time is also considered in its definition.
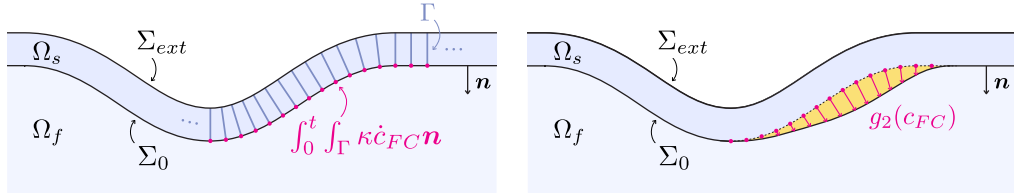

Figure 4: Schematic representation of the change in geometry of the fluid and structure domains due to the growth of plaque.

The growth on the interface $\boldsymbol{d}_G$ is extended to the fluid and structure domains Ω_f and Ω_s by means of an harmonic extension

$$-\Delta \boldsymbol{d}_{G,*} = \boldsymbol{0} \qquad \text{in } \Omega_*^t(\boldsymbol{d}_G), \qquad (14\text{a})$$
$$\boldsymbol{d}_{G,*} = \boldsymbol{d}_G \qquad \text{on } \Sigma^t(\boldsymbol{d}_G), \qquad (14\text{b})$$
$$\boldsymbol{d}_{G,*} = \boldsymbol{0} \qquad \text{elsewhere}, \qquad (14\text{c})$$

where $* = f, s$.

The resulting displacement fields $\boldsymbol{d}_{G,f}$ and $\boldsymbol{d}_{G,s}$ are applied to all points of the fluid and structure domains, respectively, to update the geometries of the lumen and the artery wall:

$$\Omega_*^t = \widehat{\Omega}_* + \boldsymbol{d}_{G,*}$$

2.6 Fixed point problem

By using the compact notation based on operators reported in Figure 2, we have that the the fluid velocity could be formally obtained by $\boldsymbol{u} = \mathcal{FS}(\Omega_f(\boldsymbol{d}_G), \Omega_s(\boldsymbol{d}_G))$, representing the FSI problem (1), whereas the three concentrations by $c_{LDL} = \mathcal{DR}(TAWSS; \Omega_s(\boldsymbol{d}_G))$,
$c_M = \mathcal{DR}(TAWSS, c_{LDL}, c_{FC}; \Omega_s(\boldsymbol{d}_G))$ and $c_{FC} = \mathcal{ODE}(c_{LDL}, c_M; \Omega_s(\boldsymbol{d}_G))$, representing (5a),(5b), and (7), respectively. Inserting (12), we have

$$c_{LDL} = \mathcal{DR}(g_1(\boldsymbol{u}); \Omega_s(\boldsymbol{d}_G)) = \mathcal{DR}(g_1(\mathcal{FS}(\Omega_f(\boldsymbol{d}_G), \Omega_s(\boldsymbol{d}_G))); \Omega_s(\boldsymbol{d}_G)) = \mathcal{C}_{LDL}(\boldsymbol{d}_G),$$

where we have introduced operator $\mathcal{C}_{LDL}$ to highlight the dependency on $\boldsymbol{d}_G$ solely. Analogously, we have

$$\begin{aligned} c_M &= \mathcal{DR}(g_1(\boldsymbol{u}), c_{LDL}, c_{FC}; \Omega_s(\boldsymbol{d}_G)) \\ &= \mathcal{DR}(g_1(\mathcal{FS}(\Omega_f(\boldsymbol{d}_G), \Omega_s(\boldsymbol{d}_G))), \mathcal{C}_{LDL}(\boldsymbol{d}_G), c_{FC}; \Omega_s(\boldsymbol{d}_G)) = \mathcal{C}_M(\boldsymbol{d}_G, c_{FC}), \end{aligned}$$

and

$$c_{FC} = \mathcal{ODE}(\mathcal{C}_{LDL}(\boldsymbol{d}_G), \mathcal{C}_M(\boldsymbol{d}_G, c_{FC}); \Omega_s(\boldsymbol{d}_G)) = \mathcal{C}_{FC}(\boldsymbol{d}_G). \tag{15}$$

Starting from (13) and inserting (15), we can compactly write the growth system of PDEs given by (1) - (5a) - (5b) - (7) - (12) - (13) as follows:

$$\boldsymbol{d}_G = g_2(\mathcal{C}_{FC}(\boldsymbol{d}_G)), \tag{16}$$

which represents a highly non-linear fixed point problem in the unknown growth function $\boldsymbol{d}_G$, which is a function of space and time.

2.7 0D Model

Equation (16) governs the evolution in space and time of the plaque thickness. An interesting question about this process is to determine if and in what conditions the plaque growth admits an equilibrium state. To answer this question we address here a simplified model derived from (1), (5a), (5b), (7), under the following simplifying assumptions:

- all fields do not depend on space;
- the artery can be described as straight cylinder of infinite length; as a result the inlet and outlet conditions are no longer relevant; we denote by R the radius, by H the thickness of the wall and by L the length of the considered portion of artery;
- the vessel walls are considered rigid;
- the plaque growth is uniform along the axis of the cylinder and axisymmetric;

11

- the outer radius of the artery is fixed, the growth takes place inward.

Under these assumptions the full model for the plaque formation reduces to a system of algebraic/differential equations in time, namely a zero-dimensional (0D) model that ultimately describes the dynamics of growth. Thanks to its simplicity, such model will be applied to study the long term behavior of the proposed plaque growth model.

The 0D model for plaque growth is composed by the following parts. The FSI problem (1) is in fact a fluid mechanics problem due to the rigid wall assumption. Then owing to the other hypotheses, we replace it with the Poiseuille flow model (a fully developed flow with parabolic profile). For such model it is straightforward to express the wall shear stress (denoted here as the Poiseuille WSS, briefly $PWSS$) as a function of the flow rate Q_{in}, the dynamic viscosity of the fluid μ_f and the radius of the artery R. Precisely we have [32],

$$PWSS = \frac{4\mu_f Q_{in}}{\pi R^3}.$$

Then we modulate the wall permeability in (11) using $PWSS$ instead of $TAWSS$.

Concerning the solute transport problems, we combine equations (5a), (5b), (6a), (6b). Starting from the variational formulation of such problems (not reported here but easily derived), testing with unit functions and reminding that all fields are spatially uniform, we obtain the following ordinary differential equations:

$$\frac{d(|\Omega_s^t|c_{LDL})}{dt} + \left(\zeta_{LDL}(|\Sigma^t| + r_{ox}|\Omega_s^t|) \right) c_{LDL} = \zeta_{LDL}|\Sigma^t|c_{LDL,f} ,$$

$$\frac{d(|\Omega_s^t|c_M)}{dt} + \left(\zeta_M(|\Sigma^t| + r_{ox}|\Omega_s^t|c_{LDL}) \right) c_M = \zeta_M|\Sigma^t|c_{M,f} ,$$

where $|\Sigma^t| = 2\pi RL$ and $|\Omega_s^t| = \pi L[(R+H)^2 - R^2]$. The equation for the foam cells remains unchanged:

$$\frac{d(|\Omega_s^t|c_{FC})}{dt} = r_{ox}|\Omega_s^t|c_{LDL}c_M .$$

Finally, in the 0D setting, the growth of the plaque is governed by a scalar function, representing its thickness and denoted as d_G. Following (13) such function becomes,

$$\frac{d}{dt}d_G = |\Sigma^t|\kappa\frac{d}{dt}c_{FC} ,$$

and it affects the inner radius of the artery as $R(t) = R_0 - d_G(t)$, being R_0 the initial radius.

Putting together all these equations, we obtain an algebraic/differential system that governs the plaque growth (expressed in terms of the variation of the inner radius) in terms of the flow rate and the blood levels of LDL and macrophages. The numerical integration of such system is simple enough to

allow for the study of its long term behavior, and how it is affected by the input parameters.

As a preliminary result of the 0D model we report in Figure 5 the evolution of solute concentrations and corresponding inner radius of the artery $R(t)$ obtained by varying a selected model parameter ($c_{LDL,f}$, that is the LDL blood concentration). These results demonstrate that the dynamical system governing the plaque growth is stable in time and allows to reach an equilibrium state. We remark that the simulation in Figure 5 covers a time span of 15 years, which would have been computationally very expensive to analyze with the complete model. However, as the 0D model lacks a spatial description of the phenomena, in Section 4 we will analyze the results of the complete 3D model, under the assumption that it inherits the same equilibrium properties of its 0D counterpart.
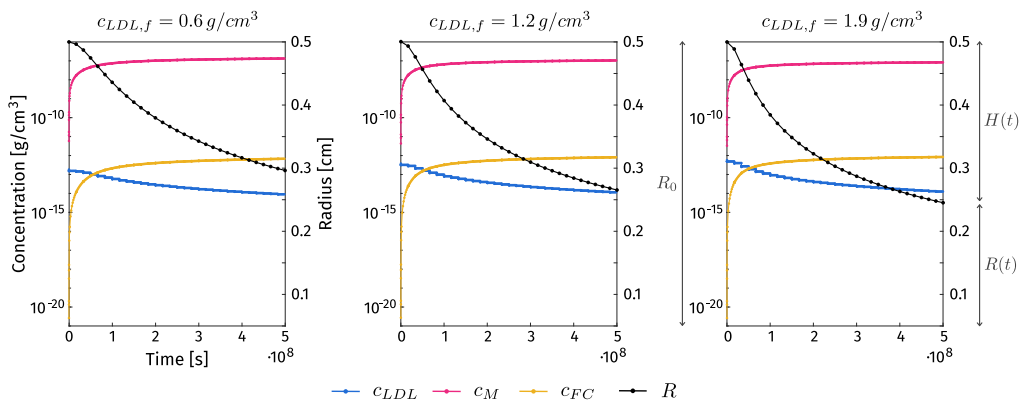

Figure 5: Time evolution in the 0D model analysis of the solute concentrations (c_{LDL}, c_M, c_{FC}) and the inner radius of the artery (R) for different values of the LDL blood concentration ($c_{LDL,f}$). The inner radius and corresponding thickness of the plaque are highlighted on the right panel.

3 Numerical methods

In order to solve the coupled problem (1) - (5a) - (5b) - (7) - (12) - (13) - (14), we propose a numerical procedure to treat the *multiscale-in-time* nature of the system. We employ a strategy based on the splitting in subproblems, i.e. FSI and solute problems, allowing the use of different temporal discretizations, adapted to the specific timescale of the subproblem, and the use of separate/pre-existing codes. This strategy is summarized in Figure 6.

Under the assumption that plaque growth is a slow process, much slower than the characteristic times typical of blood flow, we eliminate the need to solve the *short time scales* problem for the entire duration of the considered time horizon Θ. Accordingly, we divide Θ into L blocks, each comprised of
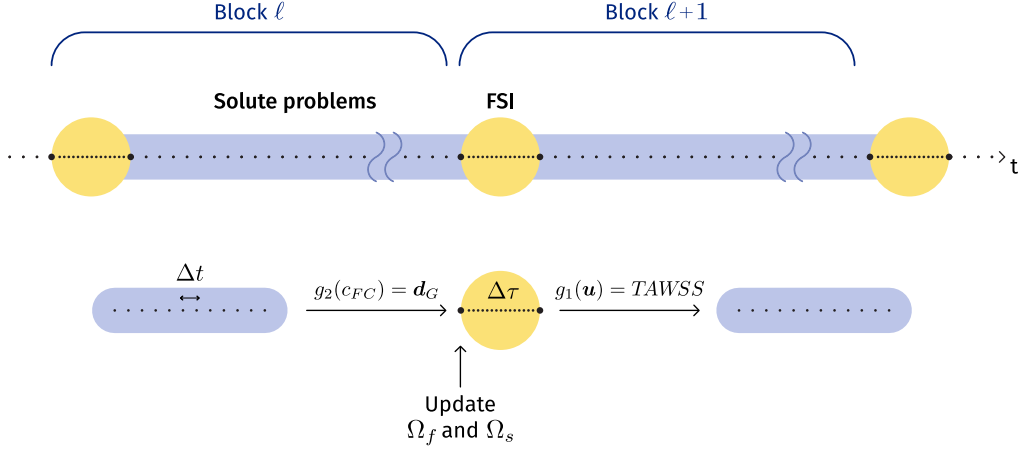
Figure 6: Schematic representation of the numerical treatment of the *multiscale-in-time* coupled problem.

two sub-blocks (*short* and *long time scales* problems). For each block ℓ the two sub-blocks are solved sequentially, each with its time discretization and simulated time duration. The functions used to couple the problems g_1 and g_2 are updated accordingly at the end of each sub-block. In doing so, the changes in the computational domains due to the plaque growth are not updated continuously, but only once they are supposed to be significant, i.e. at the end of each block. Notice however that the movement of the fluid domain within each heartbeat due to the pulsatility is updated as usual along all the FSI simulation in accordance with the ALE configuration.

In more detail, the *short time scales* sub-block (yellow regions in Figure 6) comprises subproblem (1) and is discretized in time with parameter $\Delta\tau$. It is solved for J heartbeats at the current block ℓ in the fluid and structure domains $\Omega_{f,\ell-1}$ and $\Omega_{s,\ell-1}$, obtained at the previous block $\ell-1$. After J heartbeats, *TAWSS* is computed by means of Equation (10) by considering only the last simulated heartbeat, and the values of permeability $\zeta_{LDL,\ell}$ and $\zeta_{M,\ell}$ are updated accordingly owing to (11).

The *long time scales* sub-block (blue regions in Figure 6) comprises subproblems (5a) - (5b) - (7), which are discretized in time with parameter $\Delta t \gg \Delta\tau$ and solved for K time instants in $\Omega_{f,\ell-1}$ and $\Omega_{s,\ell-1}$. At each block ℓ, the initial values of $c_{LDL,\ell}^0$, $c_{M,\ell}^0$ and $c_{FC,\ell}^0$ are set equal to the values reached at the end of the previous block $c_{LDL,\ell-1}^K$, $c_{M,\ell-1}^K$ and $c_{FC,\ell-1}^K$. After K time instants, the discretized-in-time version of the incremental growth law (13) is computed

$$\boldsymbol{d}_{G,\ell} = \int_{\Gamma(\boldsymbol{x})} \kappa \left(c_{FC,\ell}^K - c_{FC,\ell-1}^K \right) d\gamma\, \boldsymbol{n} \qquad \text{on } \Sigma(\boldsymbol{d}_G), \qquad (18)$$

allowing the update of the fluid and structure domains after the solution of (14), thus obtaining $\Omega_{f,\ell}$ and $\Omega_{s,\ell}$ at the current block ℓ.

14

After the update of the computational domains, the following block $\ell + 1$ is executed. The steps described here are detailed in Algorithm 1.

Algorithm 1 *Numerical solution of the coupled problem for plaque growth*

Let ℓ be the block index, j the heartbeat index, n the *short scales* time step index, k the *long scale* time step index.

for $\ell = 1 : L$ **do**
    for $j = 1 : J$ **do**
        for $n = 1 : N$ **do**
            Solve the discretized-in-time FSI problem at heartbeat j, time instant n:

$$\left(\boldsymbol{u}_\ell^{j,n}, p_\ell^{j,n}, \boldsymbol{d}_\ell^{j,n} \right) = \mathcal{FS} \left(\Omega_{f,\ell-1}^{j,n-1}, \widehat{\Omega}_{s,\ell-1} \right).$$

        end for
    end for
    Compute the *TAWSS*:

$$TAWSS_\ell = g_1 \left(\boldsymbol{u}_\ell \right).$$

    ....
    for $k = 1 : K$ **do**
        Solve the discretized-in-time solute problems at block ℓ, time instant k:

$$c_{LDL,\ell}^k = \mathcal{DR}^k(TAWSS_\ell; \Omega_{s,\ell-1}),$$
$$c_{M,\ell}^k = \mathcal{DR}^k(TAWSS_\ell, c_{LDL,\ell}^k, c_{FC,\ell}^{k-1}; \Omega_{s,\ell-1}),$$
$$c_{FC,\ell}^k = \mathcal{ODE}^k(c_{LDL,\ell}^k, c_{M,\ell}^k; \Omega_{s,\ell-1}).$$

    end for
    Update the fluid and structure domains:

$$\boldsymbol{d}_{G,\ell} = g_2(c_{FC,\ell}),$$
$$\Omega_{f,\ell} = \Omega_{f,0} + \boldsymbol{d}_{G,f,\ell},$$
$$\Omega_{s,\ell} = \Omega_{s,0} + \boldsymbol{d}_{G,s,\ell}.$$

end for

We discuss in what follows the numerical strategies used for the solution of the subproblems in Algorithm 1. All the strategies have been implemented in the Finite Elements library *LifeV* (`www.lifev.org`).

For the FSI problem we consider a first order time discretization for fluid, structure and kinematic interface condition (1b), with a semi-implicit treatment of the fluid convective term. The fluid geometry problem is obtained by solving an harmonic extension of the interface displacement, as common for ALE formulations [25, 17], whereas the geometric coupling (1f) is treated explicitly (i.e. using the fluid geometry of previous short scale time step). See e.g. [41, 19, 34, 35] for the accuracy and stability of this approach. The resulting linearized FSI problem is solved in a monolithic way by using P2-P1 Finite Elements, with a block approximation of the exact global Jacobian, which leads to the splitting of fluid velocity, pressure and vessel wall solutions. This strategy has been shown

to be scalable for hemodynamic problems [13, 15].

As for the three solute problems, we employ a BDF1 scheme for time discretization and P1 Finite Elements for space discretization. The linearization of the subproblem for the evolution of macrophages is obtained by an explicit treatment of c_{FC}, whereas the other non-linearities are treated by sequentially solving the 3 subproblems, see Algorithm 1.

4   Numerical results

We report in this section some 3D numerical results obtained in ideal geometries. In all experiments we consider a linear elastic material for the vessel wall, with Lamé parameters $\lambda = 9.31 \cdot 10^5 Pa$ and $\mu_s = 1.03 \cdot 10^5 Pa$, corresponding to a Young modulus $E = 3 \cdot 10^5 Pa$ and Poisson ratio $\nu = 0.45$, typical of arterial tissue. Moreover, we set $\rho_f = 1.06\, g/cm^3$, $\mu_f = 0.035\, g/cm \cdot s$ and $\rho_s = 1.20\, g/cm^3$. We point out that we consider for the grown plaque the same mechanical model and parameters as for the healthy artery wall. This is a simplified choice that, however, should not influence so much the results in a first approximation due to the limited dimensions of the plaque at the early stage.

Parameters $a_{*,1}$ and $a_{*,2}$ ($* = LDL$, M) in the expressions of permeabilities (11) are calibrated following the procedure proposed in [43] such that:

1. $\zeta_* = \zeta_*^{ref}$ if $TAWSS = WSS^{ref}$, where WSS^{ref} is a reference value of WSS computed by considering a steady Poiseuille flow in a straight pipe with radius R and mean flow rate Q [4]:

$$WSS^{ref} = \frac{4\mu_f Q}{\pi R^3} = 3.79\, Pa;$$

2. The sensitivity of the endothelium is such that the local permeability in regions with low WSS is up to a factor 25 higher than in regions with high WSS according to measurements by [24].

The resulting calibrated values and all other physical parameters for the *long time scales* model are reported in Table 1. We point out that, in order to facilitate a significant growth of plaque after only 36 months of simulated time, we chose the highest values (within the ranges reported in literature) of r_{ox} and $c_{LDL,f}$.

We set the time discretization parameters as $\Delta t = 10^5\, s$ (about 1 day) and $\Delta \tau = 10^{-3}\, s$, and choose a time horizon $\Theta = 9.6 \cdot 10^7\, s$, corresponding to 36 months. Unless specified otherwise, we simulate $L = 3$ blocks, corresponding to a simulated time for each *long time scales* problem of $3.2 \cdot 10^7\, s$ (12 months).

We tested our model in three different settings in order to investigate the influence of the initial geometry of the domain, of a subset of parameter values and of the chosen number of blocks L.

Table 1: List of physical parameters for the *long time scales* model.

Param.	Description	Value	Eq.	Ref.
D_{LDL}	Diffusivity of LDL in the wall	$3.34 \cdot 10^{-4}\ cm^2/s$	(5a)	[23]
D_M^h	Diffusivity of macrophages (M) in the healthy wall	$1.0 \cdot 10^{-9}\ cm^2/s$	(9)	[45]
D_M^d	Diffusivity of macrophages (M) in the diseased wall	$5.0 \cdot 10^{-9}\ cm^2/s$	(9)	[45]
r_{ox}	Oxidation rate of LDL in the wall	0.5	(5a)	[4]
ζ_{LDL}^{ref}	Reference permeability to LDL across the endothelium	$1.07 \cdot 10^{-11}\ cm/s$	(11)	[4]
ζ_M^{ref}	Reference permeability to monocytes (M) across the endothelium	$1.07 \cdot 10^{-12}\ cm/s$	(11)	[40]
$a_{*,1}$	Parameter modulating ζ_* ($* = LDL, M$)	$3.92\ Pa$	(11)	-
$a_{*,2}$	Parameter modulating ζ_* ($* = LDL, M$)	$0.13\ Pa$	(11)	-
$c_{LDL,f}$	Concentration of LDL in blood	$1.9 \cdot 10^{-3}\ g/cm^3$	(6a)	[22]
$c_{M,f}$	Concentration of monocytes (M) in blood	$5.0 \cdot 10^{-5}\ g/cm^3$	(6b)	[23]

4.1 Influence of initial geometry

We consider as initial geometry an ideal vessel given by a cylinder of radius $0.5\ cm$ and length $5.0\ cm$ (typical values for carotids). We consider a stenotic region, whose center is located $1.5\ cm$ far from the inlet, with three different morphologies (A, B, C), which induces the process of plaque growth in the recirculation region downstream the stenosis:

A. 60% eccentric stenosis with length $1.8\ cm$;

B. 60% eccentric stenosis with length $1.3\ cm$;

C. 50% symmetric stenosis with length $1.3\ cm$.

We observe that the use of our model, describing the early stages of plaque growth, is appropriate even in an already stenotic vessel, as plaque is initiated in the downstream region with respect to the stenosis.

In Figure 7 we report the results in terms of peak velocity streamlines, maps of $TAWSS$ and growth function $\boldsymbol{d}_{G,s}$ in the artery wall, i.e. the harmonic extension of the unknown $\boldsymbol{d}_G$ in the structure domain given by Equation (14). Peak velocity streamlines and $TAWSS$ refer to the first simulated block ($\ell = 1$), so they contain information regarding the inizialization of the plaque. As for the maps of growth, starting from the initial configuration (top row), we report in the following rows the growth reached at the end of each of the time blocks, that is each 12 months.

As a first qualitative assessment, we notice different recirculating flow structures downstream the stenosis in the three configurations. In the case of the eccentric elongated initial stenosis (configuration A), the recirculation region leads to a distribution of $TAWSS$ which induces the growth of plaque even far
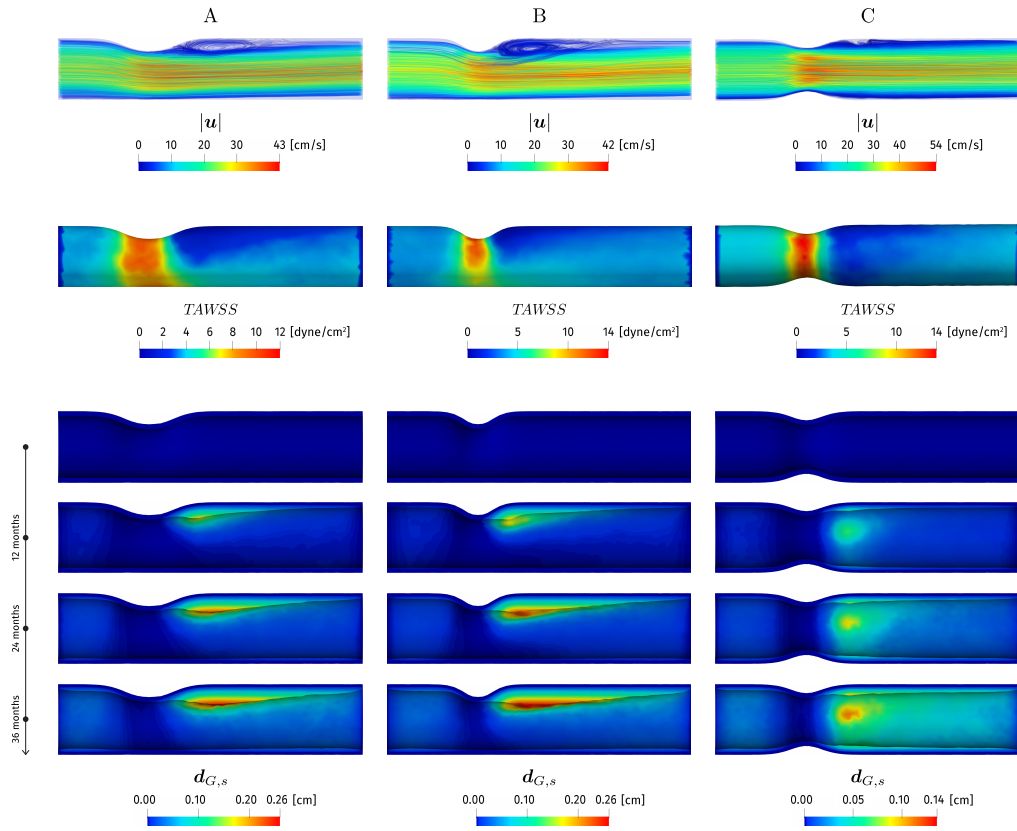
Figure 7: Top row: Peak blood velocity streamlines. Mid row: Blood *TAWSS*. Bottom rows: Maps of growth in the vessel wall ($\boldsymbol{d}_{G,s}$) obtained with different initial geometries.

from the stenosis. In configuration B, where the stenosis is more concentrated, the onset of plaque is immediately downstream the stenosis at 12 months. At 24 and 36 months, given the change in geometry due to growth, the *TAWSS* distribution resembles more closely the one of configuration A, leading to a similar final plaque morphology. As regards the symmetric stenosis (configuration C), as expected the recirculating flow structures are much smaller, leading to a thinner plaque which is distributed all along the circumference of the downstream tract.

The differences in initial geometry determine different volumes and mean thickness of the final grown plaque, reported in Table 2. Such values, far from being validated, are however significant since they fall in physiological ranges of plaque growth after 3 years [27].

Table 2: Plaque volume (cm^3) and mean thickness (cm) computed after 36 months for different initial geometries.

		Configuration		
		A	B	C
Volume	[cm^3]	0.56	0.59	0.54
Thickness	[cm]	0.12	0.14	0.07

4.2 Influence of model parameters

We investigated the differences in plaque growth due to the use of different values of a subset of parameters, such as the concentration of LDL in blood ($c_{LDL,f}$), the oxidation rate of LDL (r_{ox}) and the parameters $a_{M,1}$ and $a_{M,2}$ regulating the dependency of ζ_M on $TAWSS$. For all subsequent tests, we used the geometry corresponding to configuration A.

Reference values of $c_{LDL,f}$ taken from [22] report the concentration of LDL in blood to be near ideal when around $1.2 \cdot 10^{-3} \, g/cm^3$, very high when above $1.9 \cdot 10^{-3} \, g/cm^3$ and optimal for high risk individuals when below $0.7 \cdot 10^{-3} \, g/cm^3$. Accordingly, we simulated three scenarios: normolipidemia ($c_{LDL,f} = 1.2 \cdot 10^{-3} \, g/cm^3$), hyperlipidemia ($c_{LDL,f} = 1.9 \cdot 10^{-3} \, g/cm^3$) and hypolipidemia ($c_{LDL,f} = 0.6 \cdot 10^{-3} \, g/cm^3$).

We also investigated the influence of the rate of oxidation of LDL (r_{ox} in Equation (5a)), which also controls the differentiation of macrophages into foam cells. As different pressure levels in the bloodstream influence the oxidative stress inside the artery wall [21], varying r_{ox} corresponds to simulating the effect of different blood pressures. We employed three values: $r_{ox} = 0.5$ [4] to simulate the effect of hypertension, $r_{ox} = 0.2$ and $r_{ox} = 0.05$.

Finally, as the experimental study used for the calibration of $a_{*,1}$ and $a_{*,2}$ ($* = LDL, M$) was specific for LDL [24] and no clear reference studies were found for monocytes, we analyzed different parameter values for $a_{M,1}$ and $a_{M,2}$. We employed three sets of parameters representing three different levels of sensitivity (from the lower to the highest) of the endothelium permeability ζ_M (Equation (11)) to different values of $TAWSS$:

    i. $a_{M,1} = 4.43 \, Pa$ and $a_{M,2} = 0.63 \, Pa$;

    ii. $a_{M,1} = 4.07 \, Pa$ and $a_{M,2} = 0.27 \, Pa$;

    iii. $a_{M,1} = 3.92 \, Pa$ and $a_{M,2} = 0.13 \, Pa$ (equal to $a_{LDL,1}$ and $a_{LDL,2}$).

Figure 8 shows the plaque profiles obtained at the end of the total simulated time ($\Theta = 36$ months) for the three sets of parameters. We also report the maps of the permeability coefficient ζ_M obtained by differentiating $a_{M,1}$ and $a_{M,2}$, which refer to the first simulated block ($\ell = 1$).

As expected, growth is larger in the case of hyperlipidemia (high $c_{LDL,f}$), increased oxidative stress (high r_{ox}) and higher permeability to monocytes (set
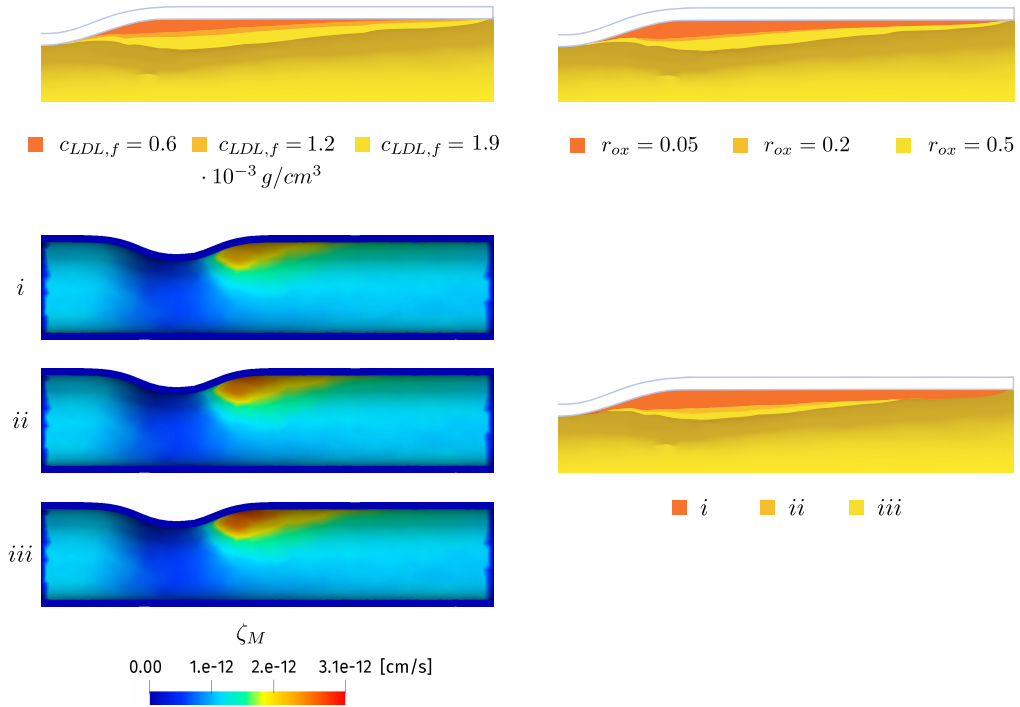
Figure 8: Final plaque profiles obtained in the case of hypolipidemia, normolipidemia and hyperlipidemia (different values of $c_{LDL,f}$, top left); hypotension, normotension and hypertension (different values of r_{ox}, top right); varying sensitivity of the endothelium permeability to monocytes (different values of $a_{M,1}$ and $a_{M,2}$, bottom right). Bottom left: maps of permeability coefficient ζ_M due to different values of $a_{M,1}$ and $a_{M,2}$.

iii for $a_{M,1}$ and $a_{M,2}$). This result is confirmed by the values reported in Table 3 regarding the plaque volume computed after 12, 24 and 36 months. Plaque growth is much more sensitive to the change of $c_{LDL,f}$ with respect to the other two parameters. Indeed, plaque volume increases by 67% and 211% when increasing the concentration of LDL in blood with respect to the hypolipidemia case. As for the other two parameters, it increases by 6% and 65% in the case of $r_{ox} = 0.5$ with respect to the smaller values considered, and by 2% and 5% in the case of set iii for $a_{M,1}$ and $a_{M,2}$ with respect to ii and i. This last result demonstrates the small sensitivity of the model to parameters $a_{M,1}$ and $a_{M,2}$. This is motivated by the values of permeability ζ_M (also reported in Figure 8), which differ by 7% and 16% at most if comparing set iii with ii and i, respectively.

4.3 Influence of number of blocks

Finally, we report the results obtained using different numbers of blocks to cover the total time of 36 months, and subsequently different coupling times between

20

Table 3: Plaque volumes (cm^3) computed after 12, 24 and 36 months for different parameter settings: hypolipidemia, normolipidemia and hyperlipidemia (different values of $c_{LDL,f}$); hypotension, normotension and hypertension (different values of r_{ox}); varying sensitivity of the endothelium permeability to monocytes (different values of $a_{M,1}$ and $a_{M,2}$).

	$c_{LDL,f}$ $[\cdot 10^{-3}\, g/cm^3]$			r_{ox} $[-]$			$a_{M,1}, a_{M,2}$ $[-]$		
	0.6	1.2	1.9	0.05	0.2	0.5	i	ii	iii
12 months	0.04	0.09	0.17	0.11	0.10	0.17	0.12	0.13	0.17
24 months	0.11	0.18	0.36	0.21	0.24	0.36	0.27	0.29	0.36
36 months	0.18	0.30	0.56	0.34	0.36	0.56	0.53	0.54	0.56

the *short* and *long time scales* problems. We employed $L = 2$, $L = 3$ and $L = 6$ blocks, corresponding to a simulated time for each *long time scales* problem of 18 months, 12 months and 6 months, respectively. Figure 9 shows the results in terms of growth function $\boldsymbol{d}_{G,s}$ in the artery wall during the whole 36 months. We also report the plaque profiles at the end of the total simulated time.

We notice that the different times of updating of the geometry, corresponding to different choices of L, influences the resulting distributions of growth. Using a longer coupling time between the *short* and *long time scales* problems (18 months, $L = 2$) results in a plaque which is concentrated immediately downstream the initial stenosis, and which protrudes into the bloodstream more than in the cases of shorter coupling times. This is due to the fact that, given the longer simulated time of the *long time scales* problem, the resulting geometric update is more accentuated. This in turn leads to a distribution of $TAWSS$, and thus growth, similar to the one shown in Section 4.1 in the case of configuration B. On the other hand, adopting a shorter coupling time (6 months, $L = 6$) leads to a smaller and more distributed growth, given the less extreme changes in blood recirculation patterns due to each geometric update.

To confirm this aspect, we report in Table 4 the values of plaque volume computed after each block. The plaque developed in the case $L = 6$ is much smaller, and with a smaller mean thickness ($0.08\, cm$) with respect to the other two cases. For $L = 2$ the total volume is smaller than for $L = 3$, but the mean thickness is slightly higher ($0.13\, cm$ and $0.12\, cm$, respectively), which confirms the growth of a thicker but more concentrated plaque.

5 Conclusions

In this work we presented a mathematical model of atherosclerotic plaque growth, which involves both macroscopic cardiovascular processes and molecular and cellular events. In order to treat the *multiscale-in-space* nature of the process of plaque growth, a fluid-structure interaction problem, arising between blood and
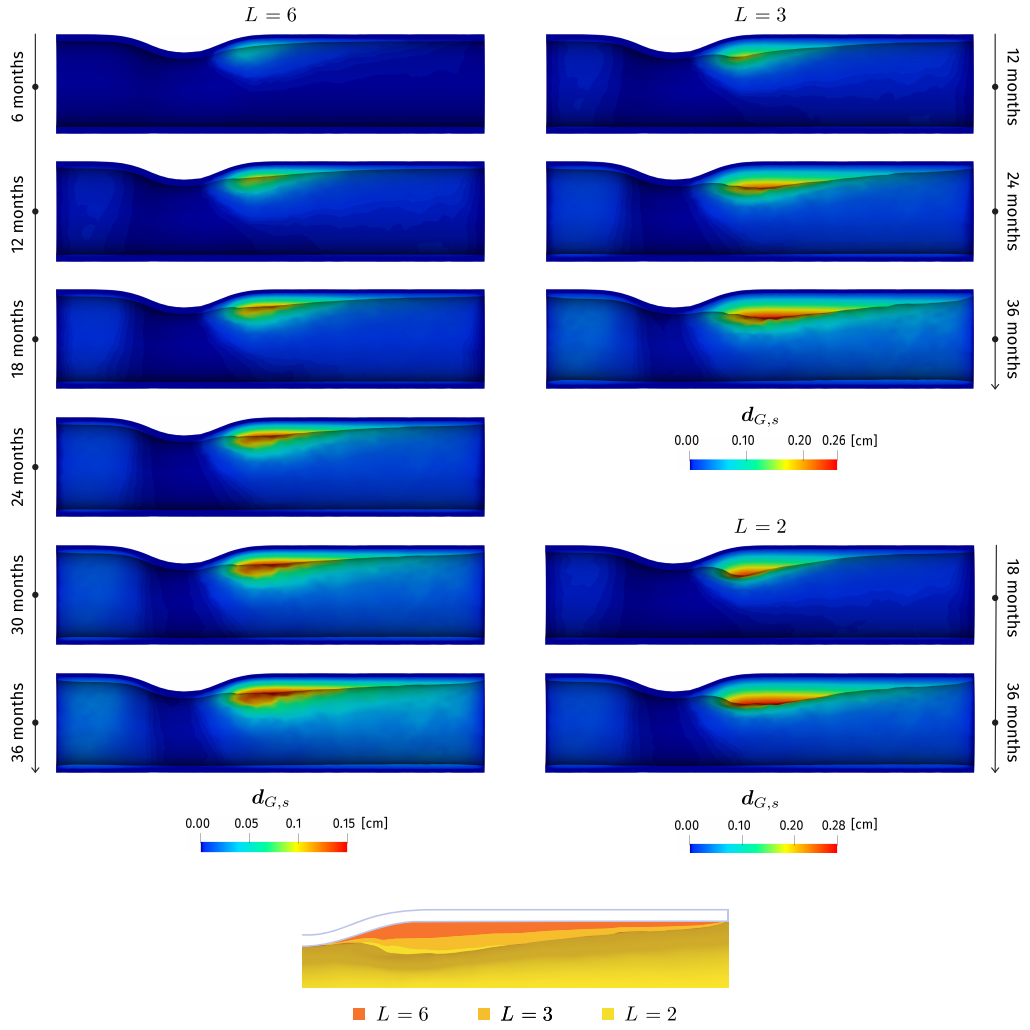
Figure 9: Top: Maps of growth ($\boldsymbol{d}_{G,s}$) obtained with different numbers of blocks L. Left column: $L = 6$. Right column, top: $L = 3$. Right column, bottom: $L = 2$. Bottom: plaque profiles after 36 months.

Table 4: Plaque volumes (cm^3) computed for different numbers of blocks L.

	$L = 2$	$L = 3$	$L = 6$
6 months	-	-	0.04
12 months	-	0.17	0.10
18 months	0.24	-	0.16
24 months	-	0.36	0.22
30 months	-	-	0.29
36 months	0.48	0.56	0.37

the artery wall, was coupled to a set of PDEs and an ODE describing the evolution of solute concentrations. The *multiscale-in-time* nature of the atherosclerotic process was treated with a suitable splitting and sequential solution of the two subproblems, which allowed to separate the short and long time scales. The coupling between the subproblems was obtained through the use of a *TAWSS*-dependent permeability of the endothelium to describe the inflow of solutes from the bloodstream. This led to a local accumulation of the involved species (LDL, macrophages and foam cells). A further coupling was introduced to update the geometric domains due to the growth of plaque caused by foam cells.

We tested our model in an ideal geometry to assess its ability to produce significant plaque growth. We investigated the effect of the initial geometry, of a subset of model parameters and of different coupling timings. In particular, we found that the frequency of geometric update due to growth influences the morphology and volume of plaque as much as the choice of different parameters, thus highlighting the importance of employing a suitable *multiscale-in-time* strategy.

References

[1] A. Arzani. Coronary artery plaque growth: A two-way coupled shear stress–driven model. *International Journal for Numerical Methods in Biomedical Engineering*, 36, 12 2019.

[2] N. Avgerinos and P. Neofytou. Mathematical modelling and simulation of atherosclerosis formation and progress: A review. *Annals of Biomedical Engineering*, 47, 04 2019.

[3] A. Brown, Z. Teng, P. Evans, J. Gillard, H. Samady, and M. Bennett. Role of biomechanical forces in the natural history of coronary atherosclerosis. *Nature reviews. Cardiology*, 13, 01 2016.

[4] V. Calvez, J. Houot, N. Meunier, A. Raoult, and G. Rusnakova. Mathematical and numerical modeling of early atherosclerotic lesions. *ESAIM: Proceedings*, 30, 2010.

[5] C. Caro, J. Fitz-Gerald, and R. Schroter. Arterial wall shear and distribution of early atheroma in man. *Nature*, 223:1159–60, 10 1969.

[6] A. Chalmers, A. Cohen, C. Bursill, and M. Myerscough. Bifurcation and dynamics in a mathematical model of early atherosclerosis : How acute inflammation drives lesion development. *Journal of mathematical biology*, 71, 03 2015.

[7] D. Chappell, S. Varner, R. Nerem, R. Medford, and R. Alexander. Oscillatory shear stress stimulates adhesion molecule expression in cultured human endothelium. *Circulation research*, 82:532–9, 03 1998.

[8] Y. Chatzizisis, A. Coşkun, M. Jonas, E. Edelman, C. Feldman, and P. Stone. Role of endothelial shear stress in the natural history of coronary atherosclerosis and vascular remodeling: molecular, cellular, and vascular behavior. *Journal of the American College of Cardiology*, 49:2379–2393, 07 2007.

[9] J.-J. Chiu, S. Usami, and S. Chien. Vascular endothelial responses to altered shear stress: Pathologic implications for atherosclerosis. *Annals of medicine*, 41:19–28, 07 2008.

[10] I. Cicha, M. Goppelt-Struebe, A. Yilmaz, W. Daniel, and C. Garlichs. Endothelial dysfunction and monocyte recruitment in cells exposed to non-uniform shear stress. *Clinical hemorheology and microcirculation*, 39:113–9, 01 2008.

[11] M. Cilla, E. Peña, and M. Martínez. Mathematical modelling of atheroma plaque formation and development in coronary arteries. *Journal of the Royal Society, Interface / the Royal Society*, 11:20130866, 2014.

[12] A. Corti, C. Chiastra, M. Colombo, M. Garbey, F. Migliavacca, and S. Casarin. A fully coupled computational fluid dynamics – agent-based model of atherosclerotic plaque development: Multiscale modeling framework and parameter sensitivity analysis. *Computers in Biology and Medicine*, 118:103623, 01 2020.

[13] P. Crosetto, S. Deparis, G. Fourestey, and A. Quarteroni. Parallel algorithms for fluid-structure interaction problems in haemodynamics. *SIAM J. Sci. Comput.*, 33:1598–1622, 2011.

[14] K. Cunningham and A. Gotlieb. The role of shear stress in the pathogenesis of atherosclerosis. *Laboratory investigation; a journal of technical methods and pathology*, 85:9–23, 02 2005.

[15] S. Deparis, D. Forti, G. Grandperrin, and A. Quarteroni. Facsi: A block parallel preconditioner for fluid-structure interaction in hemodynamics. *J. Comput. Physics*, (327):700–718, 2016.

[16] G. Di Tomaso, V. Diaz-Zuccarini, and C. Pichardo-Almarza. A multiscale model of atherosclerotic plaque formation at its early stage. *IEEE transactions on bio-medical engineering*, 58:3460–3, 2011.

[17] J. Donea, S. Giuliani, and J. Halleux. An arbitrary lagrangian-eulerian finite element method for transient dynamic fluid-structure interactions. *Computer Methods in Applied Mechanics and Engineering*, 33:689–723, 09 1982.

[18] D. Faxon, V. Fuster, P. Libby, J. Beckman, W. Hiatt, R. Thompson, J. Topper, B. Annex, J. Rundback, R. Fabunmi, R. Robertson, and J. Loscalzo.

Atherosclerotic vascular disease conference: Writing group iii: pathophysiology. *Circulation*, 109:2617–25, 07 2004.

[19] M. Fernández, J. Gerbeau, and C. Grandmont. A projection semi-implicit scheme for the coupling of an elastic structure with an incompressible fluid. *Int. J. Num. Methods Engrg.*, 69(4):794–821, 2007.

[20] C. Figueroa, S. Baek, C. Taylor, and J. Humphrey. A computational framework for fluid-solid-growth modeling in cardiovascular simulations. *Computer methods in applied mechanics and engineering*, 198:3583–3602, 09 2009.

[21] J. González Montero, N. Valls, R. Brito, and R. Rodrigo. Essential hypertension and oxidative stress: New insights. *World journal of cardiology*, 6:353–66, 06 2014.

[22] S. M. Grundy, N. J. Stone, A. L. Bailey, C. Beam, K. K. Birtcher, R. S. Blumenthal, L. T. Braun, S. de Ferranti, J. Faiella-Tommasino, D. E. Forman, R. Goldberg, P. A. Heidenreich, M. A. Hlatky, D. W. Jones, D. Lloyd-Jones, N. Lopez-Pajares, C. E. Ndumele, C. E. Orringer, C. A. Peralta, J. J. Saseen, S. C. Smith, L. Sperling, S. S. Virani, and J. Yeboah. 2018 aha/acc/aacvpr/aapa/abc/acpm/ada/ags/apha/aspc/nla/pcna guideline on the management of blood cholesterol: Executive summary: A report of the american college of cardiology/american heart association task force on clinical practice guidelines. *Journal of the American College of Cardiology*, 73(24):3168 – 3209, 2019.

[23] W. Hao and A. Friedman. The ldl-hdl profile determines the risk of atherosclerosis: A mathematical model. *PloS one*, 9:e90497, 03 2014.

[24] R. Herrmann, R. Malinauskas, and G. Truskey. Characterization of sites with elevated ldl permeability at intercostal, celiac, and iliac branches of the normal rabbit aorta. *Arteriosclerosis and thrombosis : a journal of vascular biology / American Heart Association*, 14:313–23, 03 1994.

[25] C. Hirt, A. Amsden, and J. Cook. An arbitrary lagrangian-eulerian computing method for all flow speeds. *Journal of Computational Physics*, 14:227–253, 03 1974.

[26] J. Hwang, A. Saha, Y. C. Boo, G. Sorescu, J. Mcnally, S. Holland, S. Dikalov, D. Giddens, K. Griendling, D. Harrison, and H. Jo. Oscillatory shear stress stimulates endothelial production of o 2- from p47phox-dependent nad(p)h oxidases, leading to monocyte adhesion. *The Journal of biological chemistry*, 278:47291–8, 12 2003.

[27] S. Kiechl and J. Willeit. The natural course of atherosclerosis : Part i: Incidence and progression. *Arteriosclerosis, thrombosis, and vascular biology*, 19:1484–90, 07 1999.

25

[28] D. Ku, D. Giddens, C. Zarins, and S. Glagov. Pulsatile flow and atherosclerosis in the human carotid bifurcation - positive correlation between plaque location and low and oscillating shear-stress. *Arteriosclerosis (Dallas, Tex.)*, 5:293–302, 05 1985.

[29] B. Kwak, M. Bäck, M.-L. Bochaton-Piallat, G. Caligiuri, M. Daemen, P. Davies, I. Hoefer, P. Holvoet, H. Jo, R. Krams, S. Lehoux, C. Monaco, S. Steffens, R. Virmani, C. Weber, J. Wentzel, and P. Evans. Biomechanical factors in atherosclerosis: Mechanisms and clinical implications. *European heart journal*, 35, 09 2014.

[30] P. Libby. Inflammation in atherosclerosis. *Arteriosclerosis, thrombosis, and vascular biology*, 32:2045–51, 09 2012.

[31] B. Liu and D. Tang. Computer simulations of atherosclerotic plaque growth in coronary arteries. *Molecular & cellular biomechanics : MCB*, 7:193–202, 12 2010.

[32] W. Nichols, M. O'Rourke, and C. Vlachopoulos, editors. *McDonald's Blood Flow in Arteries*. Hodder Arnold, 2011.

[33] A. Nixon, M. Gunel, and B. Sumpio. The critical role of hemodynamics in the development of cerebral vascular disease: A review. *Journal of neurosurgery*, 112:1240–53, 11 2009.

[34] F. Nobile, M. Pozzoli, and C. Vergara. Time accurate partitioned algorithms for the solution of fluid-structure interaction problems in haemodynamics. *Computers and Fluids*, 86, 11 2013.

[35] F. Nobile, M. Pozzoli, and C. Vergara. Inexact accurate partitioned algorithms for fluid-structure interaction problems with finite elasticity in haemodynamics. *Journal of Computational Physics*, 273:598–617, 2014.

[36] F. Nobile and C. Vergara. An effective fluid-structure interaction formulation for vascular dynamics by generalized robin conditions. *SIAM J. Scientific Computing*, 30:731–763, 01 2008.

[37] A. Parton, V. Mcgilligan, M. O'Kane, F. Baldrick, and S. Watterson. Computational modelling of atherosclerosis. *Briefings in bioinformatics*, 17, 10 2015.

[38] S. Pozzi and C. Vergara. (in press) Mathematical and numerical models of atherosclerotic plaque progression in carotid arteries. *Numerical Mathematics and Advanced Applications ENMATH 2019*.

[39] R. Ross. Atherosclerosis — an inflammatory disease. *American heart journal*, 138:S419–20, 12 1999.

[40] T. Silva, W. Jäger, M. Neuss-Radu, and A. Sequeira. Modeling of the early stage of atherosclerosis with emphasis on the regulation of the endothelial permeability. *Journal of Theoretical Biology*, 496:110229, 04 2020.

[41] E. Swim and P. Seshaiyer. A nonconforming finite element method for fluid-structure interaction problems. *Comput. Methods Appl. Mech. Engrg.*, 195(17–18):2088–2099, 2006.

[42] J. Tarbell. Mass transport in arteries and the localization of atherosclerosis. *Annual review of biomedical engineering*, 5:79–118, 02 2003.

[43] M. Thon, A. Hemmler, A. Glinzer, M. Mayr, M. Wildgruber, A. Zernecke-Madsen, and M. Gee. A multiphysics approach for modeling early atherosclerosis. *Biomechanics and Modeling in Mechanobiology*, 17, 2017.

[44] O. Traub and B. Berk. Laminar shear stress : Mechanisms by which endothelial cells transduce an atheroprotective force. *Arteriosclerosis, thrombosis, and vascular biology*, 18:677–85, 06 1998.

[45] Y. Yang, M. Jager, W.and Neuss-Radu, and T. Richter. Mathematical modeling and simulation of the evolution of plaques in blood vessels. *Journal of mathematical biology*, 72, 2015.

[46] C. Zarins, D. Giddens, B. Bharadvaj, V. Sottiurai, R. Mabon, and S. Glagov. Carotid bifurcation atherosclerosis. quantitative correlation of plaque localization with flow velocity profiles and wall shear stress. *Circulation research*, 53:502–14, 11 1983.

[47] T. Zohdi, G. Holzapfel, and S. Berger. A phenomenological model for atherosclerotic plaque growth and rupture. *Journal of theoretical biology*, 227:437–43, 2004.

MOX Technical Reports, last issues

60/2020   Lupo Pasini, M; Perotto, S.
Hierarchical model reduction driven by a Proper Orthogonal Decomposition for parametrized advection-diffusion-reaction problems

55/2020   Botti, M.; Castanon Quiroz, D.; Di Pietro, D.A.; Harnist, A.
A Hybrid High-Order method for creeping flows of non-Newtonian fluids

56/2020   Botti, L.; Botti, M.; Di Pietro, D. A.;
A Hybrid High-Order method for multiple-network poroelasticity

57/2020   Regazzoni, F.; Quarteroni, A.
An oscillation-free fully partitioned scheme for the numerical modeling of cardiac active mechanics

58/2020   Beraha, M.; Pegoraro, M.; Peli, R.; Guglielmi, A
Spatially dependent mixture models via the Logistic Multivariate CAR prior

59/2020   Massi, M.C.; Franco, N.R; Ieva, F.; Manzoni, A.; Paganoni, A.M.; Zunino, P.
High-Order Interaction Learning via Targeted Pattern Search

54/2020   Arnone, E.; Bernardi, M. S.; Sangalli, L. M.; Secchi, P.
Analysis of Telecom Italia mobile phone data by space-time regression with differential regularization

53/2020   Arnone, E.; Kneip, A.; Nobile, F.; Sangalli, L. M.
Some numerical test on the convergence rates of regression with differential regularization

52/2020   Arnone, E.; Kneip, A.; Nobile, F.; Sangalli, L. M.
Some first results on the consistency of spatial regression with partial differential equation regularization

51/2020   Ferraccioli, F.; Sangalli, L. M.; Arnone, E.,; Finos, L.
A functional data analysis approach to the estimation of densities over complex regions